Cerebral Cortex, November 2017;27: 5083–5094

doi: 10.1093/cercor/bhw292
Advance Access Publication Date: 24 September 2016
Original Article

ORIGINAL ARTICLE

Where does TMS Stimulate the Motor Cortex? Combining Electrophysiological Measurements and Realistic Field Estimates to Reveal the Affected Cortex Position

Andreas Bungert[2], André Antunes[2], Svenja Espenhahn[2,4], and Axel Thielscher[1,2,3]

[1]Danish Research Center for Magnetic Resonance, Centre for Functional and Diagnostic Imaging and Research, Copenhagen University Hospital Hvidovre, 2650 Hvidovre, Denmark, [2]Max Planck Institute for Biological Cybernetics, 72076 Tübingen, Germany, [3]Department of Electrical Engineering, Technical University of Denmark, 2800 Kgs. Lyngby, Denmark, and [4]Institute of Neurology, University College London, London, WC1E 6BT, UK

Address correspondence to Dr Axel Thielscher, Danish Research Center for Magnetic Resonance, Copenhagen University Hospital Hvidovre, DK-2650 Hvidovre, Denmark. Email: axelt@drcmr.dk

Abstract

Much of our knowledge on the physiological mechanisms of transcranial magnetic stimulation (TMS) stems from studies which targeted the human motor cortex. However, it is still unclear which part of the motor cortex is predominantly affected by TMS. Considering that the motor cortex consists of functionally and histologically distinct subareas, this also renders the hypotheses on the physiological TMS effects uncertain. We use the finite element method (FEM) and magnetic resonance image-based individual head models to get realistic estimates of the electric field induced by TMS. The field changes in different subparts of the motor cortex are compared with electrophysiological threshold changes of 2 hand muscles when systematically varying the coil orientation in measurements. We demonstrate that TMS stimulates the region around the gyral crown and that the maximal electric field strength in this region is significantly related to the electrophysiological response. Our study is one of the most extensive comparisons between FEM-based field calculations and physiological TMS effects so far, being based on data for 2 hand muscles in 9 subjects. The results help to improve our understanding of the basic mechanisms of TMS. They also pave the way for a systematic exploration of realistic field estimates for dosage control in TMS.

Key words: field calculations, finite element method, motor cortex, spatial targeting, transcranial magnetic stimulation

Introduction

Stimulation of the motor cortex has been the mainstay of transcranial magnetic stimulation (TMS) research since the first demonstration of this method in 1985 (Barker and Jalinous 1985). Assessment of the stimulation effects is straightforward in this case as the resulting muscle responses can be easily recorded using electromyography (EMG). The development of a large variety of stimulation protocols such as paired-pulse TMS, regular and patterned repetitive TMS, or paired associative stimulation was done in studies that targeted the motor

cortex (Kujirai et al. 1993; Pascual-Leone et al. 1994; Stefan et al. 2000; Huang et al. 2005). Most of our understanding of the physiological effects of TMS on the microscopic level stems from sophisticated experiments targeting the motor cortex (Di Lazzaro et al. 2008). Very surprisingly, however, it is still unclear which part of M1 is stimulated by TMS when a muscle twitch is elicited (e.g., Thielscher et al. 2011 vs. Fox et al. 2004). Considering that the human primary motor cortex is subdivided in histologically and functionally specific subareas (Geyer et al. 1996, 2000) that also differ in their connection patterns (Rathelot and Strick 2009), the uncertainty on the exact stimulation position thus renders many of the conclusions drawn from the aforementioned experiments uncertain. It also hampers the further development of TMS as a tool with reliable and predictable effects on brain activity.

Up to now, rather coarse approximations are used to characterize the likely targeted area, lacking a good understanding of the exact site and size of the brain tissue affected by TMS. For example, when using neuronavigation systems, only the projection of the coil center on the brain surface is usually taken for controlling the coil position. Accurate electric field calculations might help to overcome these shortcomings by delivering quantitative values with a clear physical meaning that can be compared across brain regions and individuals. Over the last years, the methods for field calculations have been improved and now allow taking the individual anatomy of the brain and head into account based on structural magnetic resonance images (MRIs). Combined with mappings of the EMG responses of finger muscles, they can be used to test for the relationship between the physiological stimulation effects and the calculated fields in different parts of the motor cortex. This combined approach might thus help to resolve long-standing uncertainties on the cortical stimulation position.

It is not well understood which neural elements in the cortex are most susceptible to TMS. Different assumptions have been made for a "neural excitability function" that links the neural excitation to the induced electric fields. They have resulted in competing hypotheses on the most likely stimulated part of the motor cortex. Assuming that, to a first approximation, the electric field strength is the most important factor determining whether a patch of cortex is excited by TMS, we have suggested that stimulation might occur in the region of the gyral crown (Thielscher et al. 2011). In contrast, it was argued that only the field component that is locally normal to the cortical sheet is effective in exciting the cortex, so that TMS would act on the neurons in the sulcal wall (Fox et al. 2004). Here, we compared the variations in the calculated electric fields in the brain with the corresponding variations in the motor threshold (MT) recorded from small hand muscles when systematically rotating the TMS coil above the hand knob region of the motor region (Fig. 1A). We tested the correspondence between 1) MT and the electric field strength as well as the correspondence between 2) MT and the field component that is locally normal to the cortical sheet. These assessments were performed in regions-of-interest (ROI) corresponding to the crown of the hand knob area of the precentral gyrus and its posterior sulcal part (Fig. 1B). This approach allowed us to validate the simulation results by testing for systematic relations between changes in the physiological response to TMS and the field estimates, while at the same time narrowing down the likely stimulated subregion. Thus, our study helps to resolve a fundamental uncertainty on the cortical position stimulated by TMS and is an important step to pave the way for a more systematic targeting and dosage approach for TMS that is based on quantitative electric field estimates.

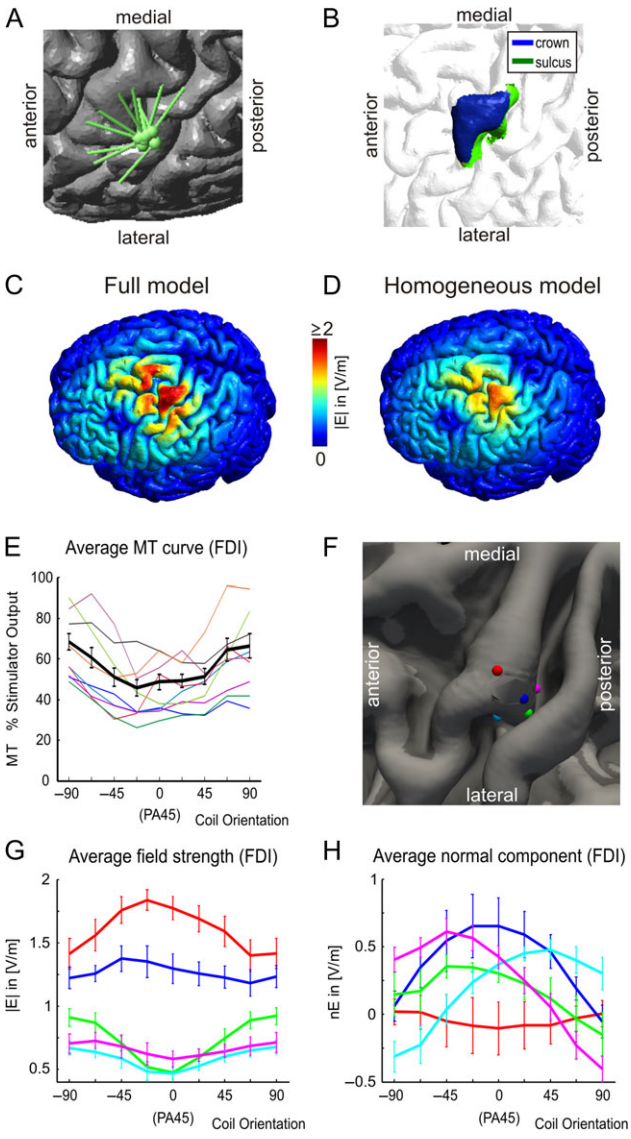

Figure 1. (*A*) Visualization of the 9 tested coil orientations superimposed over the reconstructed cortical sheet of an exemplary subject. The green dots indicate the coil centers and the lines show the coil orientations, corresponding to the approximate directions of current flow underneath the coil center. (*B*) Individual GM ROIs for a different subject. The 2 ROIs comprise the crown (blue) and the posterior sulcal part (green) of the hand knob area of the precentral gyrus. (*C*) Distribution of the electric field strength in GM, calculated using the full head model for a fixed stimulation intensity of 1 A/μs. (*D*) As in C, but using a model in which the region inside the skull was treated as homogeneous. (*E*) The black line shows the average (±SE) MT curve for the FDI across subjects. The colored lines show the corresponding MT curves of the single subjects. (*F*) Example positions selected for visualizing the electric fields (see next 2 subfigures). Red: CoG projection of the FDI; Blue: position at the posterior rim of the precentral gyrus; Green: sulcal position at the most posterolateral part of the hand knob. Light blue: sulcal position on the lateral side of the hand knob; Purple: sulcal position on the medial side of the hand knob. (*G*) Average electric field strength (±SE across subjects) in the example positions in dependence on coil orientation, calculated for a fixed stimulation intensity of 1 A/μs. The colors of the curves match the colors of the corresponding positions as shown in F. (*H*) Average of the electric field component normal to the cortical sheet (±SE across subjects), in dependence on coil orientation. The values were assessed in the example positions, calculated for a fixed stimulation intensity of 1 A/μs.

Materials and Methods

General Procedure

Eleven healthy, right-handed volunteers (age 22–44 years, 5 female) participated in the study. None of them had a history of neurological or psychiatric diseases or was on regular medication. Written informed consent was obtained from each participant prior to the first experiment. The study was approved by the local ethics committee of the Medical Faculty of the University of Tübingen. Two subjects were excluded from the final analysis (further information is given in the section on TMS below). Each participant attended 1 MRI session followed by 3 TMS sessions. The TMS sessions were separated by 1 week or more.

Magnetic Resonance Imaging: Acquisition and Analysis

MR imaging was performed using a 3T Siemens TIM Trio equipped with a 12 channel head coil. High-resolution T1- and T2-weighted structural images of the head were acquired (MPRAGE: 192 sagittal slices, matrix size=256 × 256, voxel size = 1 × 1 × 1 mm³, TR/TE/TI = 2300/2.94/1100 ms with selective water excitation, flip angle 9°; TSE: 96 sagittal slices, matrix size = 256 × 256, voxel size = 1 × 1 × 2 mm^3, flip angle 110°, TR/TE = 12770/90 ms, turbo factor 11) for building the head models used in the field calculations. The T1-weighted image was also used in the neuronavigation system to control the TMS coil position.

Diffusion MRI (dMRI) was acquired using a twice refocused SE-EPI sequence (60 axial slices, matrix size = 96 × 96, voxel size 2.3 × 2.3 × 2.3 mm³, TR/TE = 8400/96 ms, FA 90°, GRAPPA acceleration factor 2) with 62 diffusion directions and a *b*-value of 1200 s/mm². Eleven additional images with $b = 0$ s/mm² were acquired at the beginning of the sequence. The standard Siemens GE field mapping sequence (60 axial slices, matrix size = 76 × 76, voxel size 2.5 × 2.5 × 2.5 mm³, TR/TE1/TE2 = 660/5.19/7.65, FA 60°) was recorded and used for correction of static distortions in the dMRI images. The diffusion tensors were reconstructed using FSL tools (FSL fugue, eddy, and dtifit; http://fsl.fmrib.ox.ac.uk/fsl/fslwiki) and used for the estimation of the conductivity anisotropy in the brain, as described below (Opitz et al. 2011).

The individual representations of the index and little fingers of the right hand were determined using functional MRI (fMRI) based on GE EPI (20 axial slices of the upper part of the brain, 76 × 76 in plane, voxel size 2.5 × 2.5 × 2.5 mm³, TR/TE = 1395/35 ms, FA 79°, 660 volumes) to measure blood oxygen level-dependent activity during a finger tapping task that was paced by visual stimulation at 1.6 Hz. Whole-brain EPI with the same parameters, but with 60 slices and an adjusted TR of 4150 ms, was recorded to facilitate the accurate registration of the EPI data to the individual T1-weigthed image. Analysis of the fMRI data was performed using FSL Feat version 6.0. The EPI time series was motion corrected, high-pass filtered with a cut-off of 1/60 (0.016) Hz, brain extracted and smoothed with a Gaussian kernel with 1 mm full width at half maximum (FWHM). Given that the task induced very robust activations in the sensorimotor cortex, we chose to use a small FWHM of 1 mm to minimize the amount of crosstalk between motor and somatosensory activations. Registration onto the individual T1-weighted image was performed by concatenating 2 steps. The EPI time series was registered onto the whole-brain EPI using 3 translational degrees-of-freedom (DoF) and the whole-brain EPI was registered onto the T1 image based on a boundary-based registration approach (Greve and Fischl 2009). Both the EPI time series and the whole-brain EPI were corrected for static distortions based on the field map.

The paradigm consisted of a block design in which 10 s of movement alternated with 10 s of rest. Three movement conditions alternated in a pseudorandomized fashion, namely ballistic abduction movements of 1 of the 2 fingers and movement of the whole hand. A general linear model was used to determine the brain activity for the different movement conditions. In total, 3 regressors-of-interest were defined for the index finger (named "FDI"—First Dorsal Interosseuous—according to the corresponding muscle tested in the TMS part of the study), the little finger (named ADM—Abductor Digiti Minimi), and the whole hand using boxcar functions of 10 s duration that were convolved with a gamma-shaped hemodynamic response function. To account for shifts in the onset of the hemodynamic response, temporal derivatives of the resulting time courses were included in the model as regressors-of-no-interest (Friston et al. 1997; Smith et al. 2004). After model estimation, z-statistical images were calculated for the resulting maps of the parameter estimates and a corrected statistical threshold of $P<0.05$ was applied at the cluster level based on Gaussian random field theory (Worsley et al. 1996). The threshold for each voxel within a given cluster was set to an uncorrected $P < 0.01$ (corresponding to $Z = 2.3$).

For reporting, the z-statistical images were projected into Montreal Neurological Institute (MNI) space based on a nonlinear registration of the T1-weighted structural MRI on the MNI152 template (using FSL FNIRT; http://fsl.fmrib.ox.ac.uk/fsl/fslwiki). The coordinates of the peak activations in the motor cortex region were extracted and the mean coordinates (±standard error of the mean, SE) determined. In addition, average activation maps across subjects were rendered on the FreeSurfer group template for visualization using the registration procedures described on the FreeSurfer Wiki (https://surfer.nmr.mgh.harvard.edu/fswiki/FsTutorial/FslFeatFreeSurfer).

TMS: Acquisition and Analysis

Monophasic TMS pulses were applied using a MagPro X100 stimulator (MagVenture, Denmark) with a standard figure-8 coil (MC-B70). In all experiments, the stimulation frequency was restricted to a maximum of 0.2 Hz. The coil position was continuously controlled using a neuronavigation system (Visor, ANT Neuro, Netherlands) and it was ensured that the coil plane was placed tangentially to the head surface. EMG recordings of the FDI and ADM muscles of the right hand were performed using a bipolar amplifier (Psylab EEG8, Contact Precision Instruments Inc., Boston, MA, USA) connected to a PC via an A/D converter (DAQ2205, Adlink Technology Inc., Taiwan, 5 kHz sampling rate). The signal was band-pass filtered from 1 to 400 Hz in the amplifier. Data visualization and recording was performed using custom MATLAB software (The Mathworks, Natick, MA, USA). The peak-to-peak amplitudes of the muscle evoked potentials (MEPs) were extracted within time windows of 18–35 ms after the TMS pulses.

Each participant underwent 3 successive sessions. The first session served to find the best coil positions to target the motor cortex representations of the 2 muscles. The coil was oriented so that the current flow in the brain region underneath its center was directed from posterior to anterior and perpendicular to the central sulcus. This orientation is referred to as PA45 in the following, indicating that the coil was rotated approximately 45° relative to the midline in that case. Initially, the resting motor thresholds (rMT) of the 2 muscles were determined using

"hot spot" searches followed by threshold measurements. For the latter, the standard criterion of a minimum of 5 out of 10 MEPs with amplitudes exceeding 50 μV was applied (Rossini et al. 2015). Then, a regular grid of 9 × 9 coil positions with a spacing of 1 cm was centered above the hand knob region of the precentral gyrus (Yousry et al. 1997) and the positions were saved for latter analysis. MEPs were measured using 10 stimuli at each grid position with the intensity set to 120% of the higher of the 2 rMTs. For each muscle, average MEP amplitudes were calculated for each of the tested grid positions and a center of gravity (CoG) was calculated based on average MEPs and the coil positions.

After the motor mapping, 2 subjects were excluded from the further parts of the study. One subject exhibited a very high rMT of 66% for FDI and 72% for ADM. Since the goal of this study was to test orientations other than PA45 with substantially higher stimulation intensities, this subject was not further tested. For the second subject, the motor mapping procedure resulted in an unclear response distribution with high values towards the anterior-medial edge of the map. As this precluded the calculation of a reliable CoG, this subject was also excluded. This resulted in 9 subjects for which the full dataset was acquired and analyzed.

In the second and third sessions, input–output curves were systematically measured for 9 different coil orientations during selective pre-activation of 1 of the 2 muscles. One muscle was tested per session and the order was pseudorandomized across participants.

We chose to assess motor cortex excitability during controlled muscle pre-activation as this keeps the motor system in a controlled state, thereby minimizing spontaneous excitability fluctuations in the course of the experiment. The raw EMG trace was continuously shown to the subjects who were asked to keep a pre-activation level of 200 μV (peak-to-peak), as indicated by horizontal lines superimposed on the data.

The coil center was placed at the CoG of the tested muscle and 9 coil orientations were tested in a pseudorandomized order, ranging from –90° to +90° relative to PA45 in steps of 22.5° (Fig. 1A). For each orientation, an input–output (I/O) curve was measured using 7 different intensities with 10 pulses each. In order to ensure the full sampling of the I/O curve, the tested intensities were adjusted to the approximate threshold for each orientation in pre-tests by looking for the lowest intensity eliciting a cortical silent period of 10 ms or more. The cortical silent period is easily visible in the EMG traces of preactivated muscles and has roughly similar thresholds as the active MT (Classen and Benecke 1995), allowing for a quick initial adjustment of the stimulation range. The intensity levels for the I/O curves were set to 70%, 85%, 100%, 115%, 130%, 150%, 170%, 200%, and 240% of this threshold, thus providing even relative steps between intensities. Sigmoidal functions were fitted to the measured I/O curves to robustly estimate the excitation threshold for each orientation (Thielscher and Kammer 2002).

Two different methods were used for threshold estimation in order to demonstrate the robustness of the results (see Supplementary Fig. S1 for details). First, the turning point of the sigmoidal function (corresponding to the half maximum) was used and the tangent was determined at that point. The MT was then defined as the stimulator intensity at the intersection point between the horizontal baseline (corresponding to the pre-activation level) and the tangent. The dependency of MT measured by this method on the coil orientation is depicted in Figure 1E,F. In the alternative approach, the intensity at which the sigmoidal function reached 0.5 mV was chosen as MT. The level of 0.5 mV was around twice the level of the pre-activation and could therefore be reliably extracted from the data. Both approaches resulted in very similar dependencies of MT on coil orientation (average coefficient of determination across subjects: $r^2 = 97.9 \pm 1.4\%$ SE for FDI, $r^2 = 97.5 \pm 0.7\%$ SE for ADM). For that reason, the remaining part of the analysis was solely based on the first approach. Note that our way to determine MT from I/O measurements deviates from the standard approach to estimate the active MT (Rossini et al. 2015) and was chosen to make the threshold estimates as robust as possible. It is likely that the values reported for MT here are slightly higher than those that would be obtained using the standard approach. Therefore, we would like to note that the specific way of threshold estimation does not influence the final results as long as it allows to robustly capture the MT differences between coil orientations.

Head Modeling and Field Calculations

Individual head models were reconstructed using an improved version of the SimNIBS pipeline (www.simnibs.org; Windhoff et al. 2013; Thielscher et al. 2015) based on the T1- and T2-weighted structural MR images. The final meshes contained around 500 000 nodes and 3 000 000 tetrahedral elements and distinguished between 5 tissue types, namely brain white matter (WM), gray matter (GM), cerebrospinal fluid (CSF), skull, and skin. The tissue conductivities were set to $\sigma_{skin} = 0.25$ S/m (average between outer skin and fat as given in Truong et al. 2013) $\sigma_{skull} = 0.01$ S/m (Dannhauer et al. 2011), $\sigma_{CSF} = 1.79$ S/m, $\sigma_{GM} = 0.276$ S/m, and $\sigma_{WM} = 0.126$ S/m (Thielscher et al. 2011). WM and GM were assigned anisotropic conductivities while the 3 other tissues were treated as isotropic. The conductivities of WM and GM were estimated from the diffusion tensors using a "volume normalized" approach as described in Opitz et al. (2011). It was assumed that the diffusion and conductivity tensors have the same eigenvectors (Tuch et al. 2001; Güllmar et al. 2010). The eigenvalues of the conductivity tensors were rescaled such that the mean conductivity of each tensor matched the corresponding isotropic tissue conductivities listed above. In order to characterize the impact on the induced electric field of the GM, WM, and CSF compartments inside the skull, the results obtained with the "full" head models were compared with those of simplified models with an isotropic conductivity of $\sigma_{CSF} = \sigma_{GM} = \sigma_{WM} = 0.7$ S/m for all tetrahedra inside the skull. The simplified models still accurately captured the inner shape of the skull. The results obtained with these models thus represent the "best cases" which can be obtained when using spherical head models in case the local skull shape underneath the TMS coil approaches a perfect sphere.

The electric field $\boldsymbol{E}$ was calculated by numerically solving

$$\boldsymbol{E} = -\partial \boldsymbol{A}/\partial t - \nabla \varphi, \quad (1)$$

with $\boldsymbol{A}$ being the magnetic vector potential of the TMS coil. The vector potential of the MC-B70 coil was pre-calculated using a coil model consisting of a superposition of 1248 magnetic dipoles, as described in Thielscher and Kammer (2004). The coil positions were saved in the neuronavigation system and imported into the calculations using custom-written Matlab scripts in order to accurately position the coil model relative to the head model according to the real coil position. Once the magnetic vector potential was determined, the finite element method (FEM) was used to calculate the electric potential φ at

the nodes, employing the Galerkin approach and tetrahedral first-order elements (Dular et al. 1998; Windhoff et al. 2013). The residuals for the conjugate gradient solver used to solve the resulting linear system were required to be $<10^{-9}$. The electric field $\boldsymbol{E}$ at the barycenters of the tetrahedral elements was then determined by taking the numerical gradient of φ and applying equation (1). The field was calculated for a rate of change of the coil current of 1A/μs (Fig. 1C,D shows field distributions for coil orientation PA45 for the full and homogeneous head models of an exemplary subject) and entered into the analysis described in the next section. When required for additional reporting, it was further rescaled to yield the field strength at MT (Thielscher and Kammer 2002).

Comparison of MT Data with Calculated Fields: Group Analyses

The tested conditions were motivated by complementary assumptions on the mechanisms by which TMS induces MEPs, resulting in the assessment of different target variables: 1) the electric field strength in GM, 2) the electric field strength in WM, and 3) the component of the field which is normal to the local cortex orientation. The first target variable was chosen according to the assumption that TMS predominantly activates GM, irrespective of the field orientation relative to the cortical sheet. This is the most commonly used assumption and is based on the observation that the many bends and terminals of axons in GM are likely to represent low-threshold points (Maccabee et al. 1993, 1998; Rattay 1998; Ilmoniemi et al. 1999) and do not have strong preferences in their spatial alignment. It is also supported by more recent modeling work demonstrating that several neuron types might have similar activation thresholds to TMS (Salvador et al. 2011), limiting the directional selectivity of the network of neurons in the cortical sheet to the field direction. The second target variable (i.e., the field strength in WM) was based on the hypothesis that TMS might also activate the WM part underneath the gyral crown, given that a high field strength occurs at this position (Thielscher et al. 2011) and that myelinated axons with bends and axon collaterals have been reported in that region which should possess low thresholds to TMS stimulation (Yamashita and Arikuni 2001; Salvador et al. 2011). The third target variable (i.e., the component normal to the GM surface) was based on the hypothesis put forward in Fox et al. (2004). It was triggered by the observation that TMS preferentially causes positron emission tomography (PET) activations inside the central sulcus, that is, at positions in which the field is roughly perpendicular to the cortical surface. This hypothesis is discussed in detail further below.

As the first step of the analysis, the electric field was read out in the middle of the cortical sheet of the left hemisphere using custom-written software. This was done by interpolating the electric field at the nodes constituting the surface halfway between the pial and WM surfaces, as reconstructed by FreeSurfer. Interpolation was performed with resort to a Gaussian kernel with a FWHM of 1.7 mm, using the field values determined at the barycenters of the neighboring tetrahedra. Both the electric field strength $|\boldsymbol{E}|$ and the field component $\mathbf{n}\boldsymbol{E}$ normal to the local orientation of the cortical sheet were determined. The values were then mapped on the FreeSurfer average template using FreeSurfer tools and the surface-based registration procedure implemented in FreeSurfer (Fischl et al. 1999). Average distributions across coil orientations and subjects were calculated for $|\boldsymbol{E}|$ and $\mathbf{n}\boldsymbol{E}$ at a stimulation intensity corresponding to the MT, for comparison with the fMRI activation patterns.

In addition, we were interested in determining the cortical positions in which the changes of $|\boldsymbol{E}|$ (or $\mathbf{n}\boldsymbol{E}$) with coil orientation corresponded well with the changes in the MT. When calculating $|\boldsymbol{E}|$ (or $\mathbf{n}\boldsymbol{E}$) at a fixed stimulation intensity (arbitrary choice; here: 1 A/μs) and determining its dependence on coil orientation, we expect it to be inversely related to MT changes at cortical positions which contribute to the generation of the muscle responses: The field should be strong at orientations having low MTs and vice versa weak for orientations with high MTs. That is, the product of $|\boldsymbol{E}|$ (or $\mathbf{n}\boldsymbol{E}$) and MT should ideally stay constant at cortical positions which contribute to the muscle response. The relative standard deviation (SD) of the product across coil orientations was thus used as a measure of the correspondence between the biophysical estimate and the physiological response. For convenience, the relative SD was scaled in percent and subtracted from 100%:

$$\%\mathrm{RSD}_{\mathrm{inverse}} = 100\% \cdot \left(1 - \frac{\mathrm{SD}\left(\mathrm{MT} \cdot |\boldsymbol{E}|_{1\mathrm{A}/\mu\mathrm{s}}\right)}{\mathrm{Mean}\left(\mathrm{MT} \cdot |\boldsymbol{E}|_{1\mathrm{A}/\mu\mathrm{s}}\right)}\right). \quad (2)$$

The correspondence between $\mathbf{n}\boldsymbol{E}$ and MT was calculated similarly by replacing $|\boldsymbol{E}|$ by $\mathbf{n}\boldsymbol{E}$ in the above equation. The relative SD (i.e., SD divided by the mean) was used rather than SD as the results would have been biased to positions with low average field strengths. It is worth noting that as the fields were calculated for a fixed intensity of 1 A/μs for all coil orientations, the acquired electrophysiological data was not used in the field calculations. By that, MT and electric fields were assessed fully independently from each other before being compared via equation (2). In the optimal case, the SD of the product between $|\boldsymbol{E}|$ (or $\mathbf{n}\boldsymbol{E}$) and MT approaches zero and $\%\mathrm{RSD}_{\mathrm{inverse}}$ will reach its upper limit of 100%. The reference value is given by $\%\mathrm{RSD}_{\mathrm{inverse}}$ of the MT itself (i.e., setting $|\boldsymbol{E}|$ in equation (2) to a constant value of 1). Cortical positions with a good correspondence between field and MT changes across coil orientations have a $\%\mathrm{RSD}_{\mathrm{inverse}}$ which exceeds this reference value. Note that we opted against using the correlation coefficient between $|\boldsymbol{E}|$ (or $\mathbf{n}\boldsymbol{E}$) and MT, as it normalized the covariance of the 2 variables by their individual SD. This penalizes situations in which the dependence of MT on coil orientations is not very pronounced. Even though there might be cortical positions in which the field also does not strongly depend on the orientation (indicating a good correspondence), these positions would likely get low correlation coefficients which would be dominated by the residual fluctuations around the mean values of MT and the field.

In addition to visualizing the group results on the FreeSurfer average template, the average MNI coordinates of the CoG positions of the initial TMS mapping and the positions experiencing the strongest fields and the highest $\%\mathrm{RSD}_{\mathrm{inverse}}$ values were determined. To do so, the individual CoG positions were projected on the brain surface along the direction that was locally normal to the skin surface. The transformation of the coordinates from the individual space of the surface and volume mesh to the MNI template involved 2 successive steps. First, the mesh coordinates were transformed into the space of the structural T1-weighted image based on the information given on https://surfer.nmr.mgh.harvard.edu/fswiki/CoordinateSystems. Then, a non-linear transformation from the individual T1-weighted image to the MNI template, as determined by FSL FNIRT, was applied.

Comparison of MT Data with Calculated Fields: Analyses Based on ROI

For a formal statistical analysis, average $\%RSD_{inverse}$ values were assessed in individually defined ROIs. The thresholded individual activation patterns of the finger tapping task (pooled for index and little finger movements) were projected from the EPI space to the head mesh using custom software and a nearest-neighbor lookup, thereby taking only positions within the cortical sheet into account. The selected parts of the activation patterns were situated on the crown and posterior wall of the precentral gyrus. The selected region was then divided into 2 ROIs ("crown" and "sulcus" in Fig. 1*B*) by cutting it at the height at which WM ended. In addition, 2 ROIs were created that covered the WM parts next to the selected cortical regions. A superior WM region of approximately 5 mm thickness was selected as "crown" and the underlying posterior half of the WM of the gyrus was selected as "sulcus".

The value for $\%RSD_{inverse}$ was calculated for each tetrahedron and average $\%RSD_{inverse}$ values were determined across all tetrahedra for each ROI. In order to determine the normal component **nE**, the vector normal to the closest triangle of the WM boundary was used for the calculations. The extracted average $\%RSD_{inverse}$ values were entered into 8 pre-planned paired *t*-tests to test for differences between the crown and sulcus ROIs and to compare the results for |**E**| versus **nE**. A detailed motivation of the performed comparisons can be found in the corresponding section of the Results. The test results were thresholded at a significance level of $P = 0.05$ (2-tailed, Bonferroni-corrected for multiple comparisons). In addition, trends that were significant at $P = 0.05$ (uncorrected) were reported.

In a further analysis, we explored the hypothesis that TMS stimulates different parts of the extended muscle representations, depending on coil orientation. The highest 10% of |**E**| were extracted from the cortical ROIs (combined crown and sulcus) for each coil orientation separately and the resulting values were used to calculate $\%RSD_{inverse}$. This was repeated for the normal component **nE**. Three pre-planned paired *t*-tests (2-sided, Bonferroni-corrected) were performed for comparison.

Results

Electrophysiological Measurements and Functional MRI: Summary of Findings

The cortical projections of the CoG positions as determined by the mapping procedure are visualized as blue spheres in Figure 2 and their MNI coordinates are given in Table 1. The projections are located in the hand knob region on the crown of the precentral gyrus. The CoG of the ADM is shifted slightly medially relative to that of the FDI, consistent with the known topography of the hand muscles (Raffin et al. 2015). Figure 1*E* depicts the average curve for the FDI, superimposed on the individual results (see Supplementary Fig. S1*E* for the corresponding curve for ADM). The average MTs for the PA45 orientation are 45.3 ±3.1% SE (FDI) and 43.2±4.4% SE (ADM) of maximum stimulator output (MSO). These values are in concordance with Kammer et al. (2001), which reported slightly higher values for the resting MT for the same combination of stimulator and coil. As expected, MT is clearly modulated by coil orientation, but the exact shape of the curve differs between the 2 muscles and across subjects. On average, the difference between the highest and lowest MT was 82.4% (±33.8% SD) of the lowest MT for the FDI, and 76.6% (±20.4% SD) for the ADM. Averaging the coil orientations with the lowest MT across subjects resulted in −5.6° (±33.4° SD) for the FDI and 10° (±19.8° SD) for the ADM. That is, the average of the optimal coil orientation is close to PA45 (corresponding to 0°), but it possesses a clear spread across subjects. Comparing the curves obtained for ADM and FDI revealed an average coefficient of determination across subjects of $r^2 = 65.0 \pm 9.2\%$ SE. The fMRI activations for movements of the little and index fingers overlapped strongly (Fig. 2*A*) and resulted in very similar positions for the activation peaks (Table 1). In contrast to the projections of the CoGs, the fMRI peaks were consistently found in the sulcal part of the hand knob region. This difference is in concordance with the results of a range of studies comparing TMS motor mapping with fMRI (Herwig et al. 2002; Sparing et al. 2008).

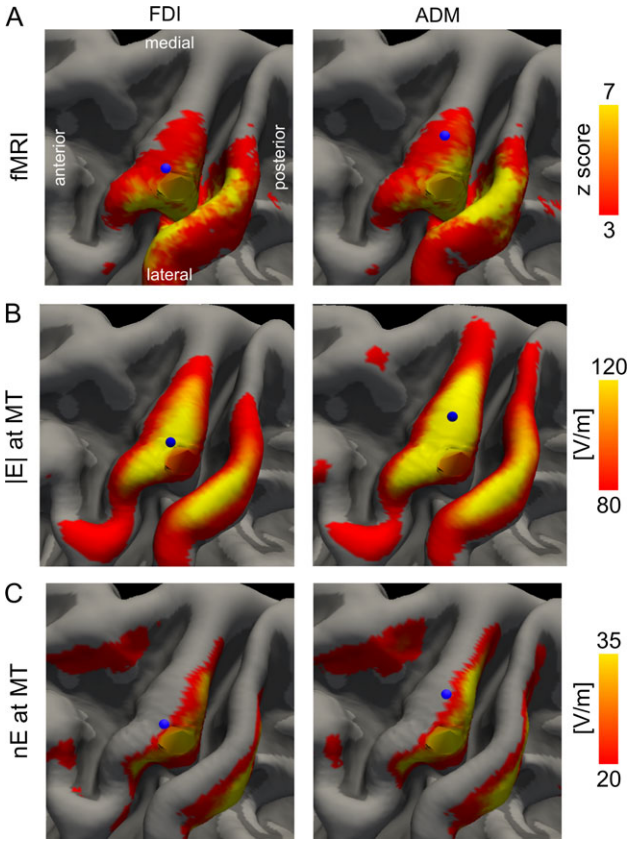

Figure 2. Group fMRI activations and field distributions in the motor cortex and surrounding areas, shown on the Freesurfer average template. The blue spheres indicate the positions of the CoG projections as listed in Table 1. Left: FDI, right: ADM. (*A*) Mean fMRI activity for voluntary movements of the index (FDI) and little (ADM) fingers. Mean *z*-scores obtained from the FSL analyses and averaged across subjects are shown (a score of 3 corresponds to a P-value of 0.001, a score of 7 to $P < 10^{-11}$). (*B*) Average distribution of the electric field strength |**E**| at MT, averaged across all orientations and subjects (calculations based on the "full" head models). (*C*) As in B, but using the positive normal component **nE** of the electric field vector relative to the cortical sheet. The comparatively low upper limit of 35 V/m stems from the fact that the spatial distribution of **nE** differs markedly across coil positions, as visible in Supplementary Figure S2*B*, thus resulting in low average values.

Spatial Distribution of the Electric Fields

The spatial distribution of the field strength |**E**| at the MT, averaged across subjects and coil orientations, is shown in Figure 2*B*. The peak field strengths occur at the crown of the

Table 1 Average coordinates in MNI space for the fMRI activation peaks in the precentral gyrus, the projections of the TMS hotspot used for the initial MT measurements onto the brain surface, the projections of the CoG onto the brain surface and the peak values of the electric field strength |**E**| and the normal component **nE** of the field relative to the gyrus

	FDI				ADM			
	X (±SE)	Y	Z	z-Value (fMRI) or [V/m] (E field)	X	Y	Z	z-Value (fMRI) or [V/m] (E field)
FMRI activation	−34.8 (±0.4)	−21.5 (±0.6)	59.5 (±0.3)	14.1 (±1.3)	−34.3 (±0.6)	−21.9 (±0.6)	60.3 (±0.2)	14.8 (±1.6)
TMS hotspot projection	−37.3 ± 3.0	−18.6 ± 2.9	65.7 ± 2.0	—	−35.2 ± 4.0	−17.8 ± 2.9	66.1 ± 2.2	—
CoG projection	−38.3 (±2.2)	−15.2 (±3.1)	67.9 (±1.3)	—	−34.2 (±2.4)	−16.1 (±1.9)	71.6 (±1.1)	—
|**E**| (MT)	−34.6 (±0.8)	−15.9 (±0.7)	65.9 (±0.6)	143 (±13.8)	−33.9 (±0.8)	−16.4 (±0.6)	66.3 (±0.7)	159.6 (±15.3)
nE (MT)	−35.8 (±0.8)	−18.9 (±0.9)	59.5 (±1.2)	90.5 (±9.2)	−35.8 (±0.8)	−19.0 (±0.9)	59.2 (±1.2)	100.0 (±9.3)
|**E**| $\%RSD_{inverse}$	−34.9 (±0.7)	−16.1 (±0.8)	61.4 (±0.6)	95.5 (±0.44)	−34.1 (±0.7)	−16.9 (±0.6)	62.3 (±0.6)	96.0 (±0.43)
nE $\%RSD_{inverse}$	−38.2 (±1.1)	−18.3 (±1.4)	60.0 (±0.8)	86 (±0.56)	−37.7 (±1.2)	−17.7 (±1.3)	61.4 (±1.9)	86.2 (±0.41)

For |**E**| and **nE**, the positions with the highest $\%RSD_{inverse}$ values are also reported. The differences of the positions of the peak values for |**E**| and the fMRI peaks in anterior–posterior (Y) and inferior–superior (Z) directions were statistically significant for both muscles.

precentral gyrus (Table 1). Note that the peak values (Table 1) are higher than previously estimated based on simplified spherical head models (Thielscher and Kammer 2002), demonstrating the impact of the brain anatomy on the field. Figure 2*C* shows the corresponding distribution for the normal component **nE** of the field vectors. The highest values occur in the posterior transition region between the crown and the sulcal part of the precentral gyrus. Compared with more sulcal positions, the field strength in this region is still high while the field orientation is already partly normal to the cortical sheet, resulting in a net maximum. The peak strength of **nE** reaches roughly 63% of that of |**E**| (Table 1). Interestingly, high values are also seen on the postcentral gyrus for both |**E**| and **nE**. Sorting the positions of the peak values along the posterior–anterior direction (Y component in Table 1) reveals a common pattern for both muscles: The peaks for |**E**| are found close to the projection of the CoGs on the crown while the peaks of **nE** are located posteriorly, but still are anterior to the fMRI activation peaks in the central sulcus.

Comparison of the Calculated Electric Fields with the Electrophysiological Results

For the FDI, Figure 1*G* depicts the dependence of |**E**| on the coil orientation for exemplary positions in the hand knob (see Fig. 1*F*). The fields were calculated for a fixed stimulation intensity (1 A/μs) so that the effect of the gyral anatomy on the field strength is clearly visible. The field in the crown of the hand knob (red curve) shows a dependence on coil orientation which is opposite to the one shown for MT in Figure 1*E*. This indicates that the value of $\%RSD_{inverse}$ will be high for this position. In contrast, the dependencies shown for the other positions are flatter or even opposite to it. The dependencies of the normal component **nE** on coil orientation are shown in Figure 1*H* for comparison. As expected, **nE** is close to zero at the crown of the hand knob (red curve) as the current flow is approximately parallel to the inner boundary of the skull. In the sulcus, **nE** has a clear dependence on coil orientation which differs for the different example positions. The large error bars indicate that the dependence of **nE** on coil orientation exhibits strong inter-individual differences. For further information, snapshots of the field distributions for each coil orientations are shown in Supplementary Figure S2.

Figure 3*A* shows the average distribution of $\%RSD_{inverse}$ of |**E**|, based on the field calculations using the "full" head models. The best correspondence between the changes in |**E**| and MT in dependence on the coil orientation occurs at positions on the crown of the precentral gyrus. These regions have a good overlap with the regions of high field strength (Fig. 2*B*). Basing the field calculations on simplified head models that do not take the gyrification pattern of the brain into account clearly changes this pattern. High values of $\%RSD_{inverse}$ are now also found in the junction area of the superior frontal sulcus and the precentral sulcus (Fig. 3*B*). Considering the low average field strength in this region, it is unlikely that it is stimulated strongly enough to contribute to the generation of the MEPs. Compared with the full head models, the field distributions estimated by the simplified head models does not fit as well to the physiological response pattern. The changes in **nE** and MT, based on calculations performed with the full head models, show very weak correspondences (Fig. 3*C*). The peak values of $\%RSD_{inverse}$ are situated in the posterior wall of the precentral gyrus and are generally much lower than those obtained for the field strength.

Quantitative comparisons between the mean values of $\%RSD_{inverse}$ in the crown and sulcus ROIs are given in Figure 4. Consistent with the qualitative results discussed above, changes in |**E**| correspond significantly better with the changes in MT in the crown ROIs versus the sulcus ROIs for both muscles (2 leftmost bars in the plots of Fig. 4*A*). The difference between both ROIs is roughly 10 "units" of $\%RSD_{inverse}$, which is substantial considering the fact that the range from no dependence between |**E**| and MT and a perfect dependence is around 20 units (from 80% as indicated by the green bars in Fig. 4*A* to 100%). Changes in **nE** are only weakly related to changes in MT (third and fourth bars in Fig. 4*A*). Importantly, however, taking |**E**| into account does not significantly increase $\%RSD_{inverse}$ relative to the $\%RSD_{inverse}$ value of the MT itself (green bars in Fig. 4*A*) in any of the cases. This indicates that the correspondence between changes of the calculated fields and of the MT is fair, but not strong even in the best case (|**E**| assessed in the crown ROIs; leftmost bars in Fig. 4*A*). Basing the analyses on the WM ROIs directly underneath (crown) or neighboring (sulcus) the GM ROIs resulted in a very similar pattern of findings (Fig. 4*B*). To summarize, variations in the electric field strength at the crown of the precentral gyrus correspond better with the variations in MT compared with most of the alternatively tested conditions. An exception is the field strength in the WM region directly underneath the crown which exhibits a similar behavior as the field strength in the crown itself.

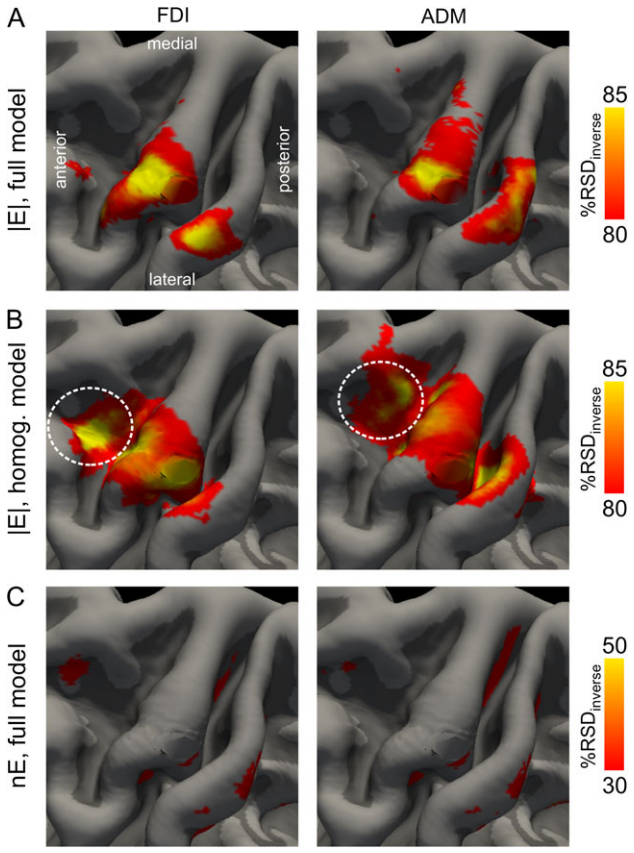

Figure 3. Topographic distribution of $\%RSD_{inverse}$ as a measure of the correspondence between changes in the local electric field strength |**E**| (or the normal component **nE**) and changes in the MT. Shown is the average across subjects on the Freesurfer template. Left: FDI, right: ADM. (*A*) Results for the electric field strength |**E**| assessed using the full head models distinguishing between GM, WM, and CSF. For both muscles, the distributions show well defined peaks at the gyral crown of the hand knob area. The lower limit of the scaling was set to 80% which approximately corresponds to the $\%RSD_{inverse}$ of MT itself (green bars in Fig. 4). Values lower than 80% indicate the absence of a correspondence between field and MT changes. (*B*) As in B, but |**E**| calculated using simplified head models with a homogeneous conductivity inside the skull. Compared with A, the distributions are much more widespread with lower peak values at the gyral crown of the hand knob and high values within the posterior part of the superior frontal gyrus (highlighted by the white dashed circles). (*C*) Results for the normal component **nE**, assessed using the full head models. The distributions are scattered and the peak values are generally low.

Finally, we tested the hypothesis that the recorded muscle responses resulted from stimulation of different subparts of the muscle representations when rotating the coil. For each coil orientation, the average of the highest 10% of the field strength values |**E**| (or of **nE**) in the combined crown and sulcus ROIs was taken, and the $\%RSD_{inverse}$ across coil orientations determined for these values. The spatial distribution of the cortical positions experiencing the highest |**E**| and **nE** are shown in Figure 4*D*,*E* on the FreeSurfer group template. The scaling indicates how often a cortical position experiences peak field values. Figure 4*D* reveals that some positions on the gyral crown consistently (for up to 7 of the 9 orientations) see strong field strengths |**E**|. The cortical positions experiencing high normal components **nE** are more scattered, with less overlap across coil orientations (Fig. 4*E*), and are placed on the posterior lip of the postcentral gyrus. The $\%RSD_{inverse}$ values based on these peak values are given in Figure 4C. The values for |**E**| are significantly higher than the reference values for MT (for the FDI only at the uncorrected level), indicating a reasonable correspondence between the changes in the peak field strength |**E**| and MT across coil orientations. The results for **nE** do not reach significance, caused by higher variance between subjects.

Discussion

The study assessed the correspondence between changes of the TMS-induced electric field and the MT when systematically varying the coil orientation. The electric field distribution was estimated using a FEM and realistic head models reconstructed from individual structural MRI data. A range of important conclusions can be drawn from the findings reported here.

First, the best correspondence was consistently seen for regions around the crown and posterior lips of the precentral gyrus, irrespective of the target variable which was read out. This was the case for the field strength in both GM and WM (Fig. 4*A*,*B*), but also for the normal component of the field when assuming that the stimulated cortex position changes with coil orientation (Fig. 4C). That is, for the different tested a priori assumptions on the link between induced electric field and neural excitation, our results robustly indicate that TMS given at threshold activates superficial parts of the brain. This is of relevance here as M1 is known to be subdivided into a rostral and a caudal part (Stepniewska et al. 1993; Geyer et al. 1996; Rathelot and Strick 2009), with the caudal part being situated deeper inside the central sulcus. The 2 parts differ histologically and functionally (Stepniewska et al. 1993; Geyer et al. 1996), and only the caudal part makes monosynaptic connections with the spinal motoneurons which innervate the finger muscles (Rathelot and Strick 2009). Considering that TMS stimulation at threshold likely affects the rostral part of M1 and maybe also the caudal part of the dorsal premotor cortex more than the caudal part of M1, this explains the occurrence of I- rather than D-waves in that case (Di Lazzaro et al. 2008). The latter would require the direct stimulation of monosynaptic connections which are only present in the deeper caudal part of M1. It is worth noting that our results apply to the activation of the excitatory inputs to corticospinal neurons and that activation of, for example, the cortical inhibitory interneurons tested by the SICI protocol (Kujirai et al. 1993) could have different rules.

Second, the results demonstrate a reasonable fit between the physiological responses to motor cortex stimulation and the field distribution calculated using realistic head models. The results encourage the further exploration of biophysical models as a method to control the "dosing" of TMS better by equalizing the field strength in the superficial region underneath the coil both across brain regions and individuals. Statistically significant results were obtained for the peak field strength in GM (Fig. 4C), suggesting that this variable is currently the best choice when investigating response-dose dependencies in future studies. It should be noted that similarly high values for the correspondences were obtained for the peak of the normal component (non-significant difference between |**E**| and **nE**, as shown in Fig. 4C). Also, the correspondences seen when assessing the field strengths in GM and WM of the gyral crown were of similar height (leftmost bars in Fig. 4A vs. *B*; the differences between GM and WM were not significant). That is, the observed correspondence was largely robust to dramatic changes in the assumptions on how TMS activates the neural tissue. Our results confirm and extend the findings of earlier studies which tested the correspondence

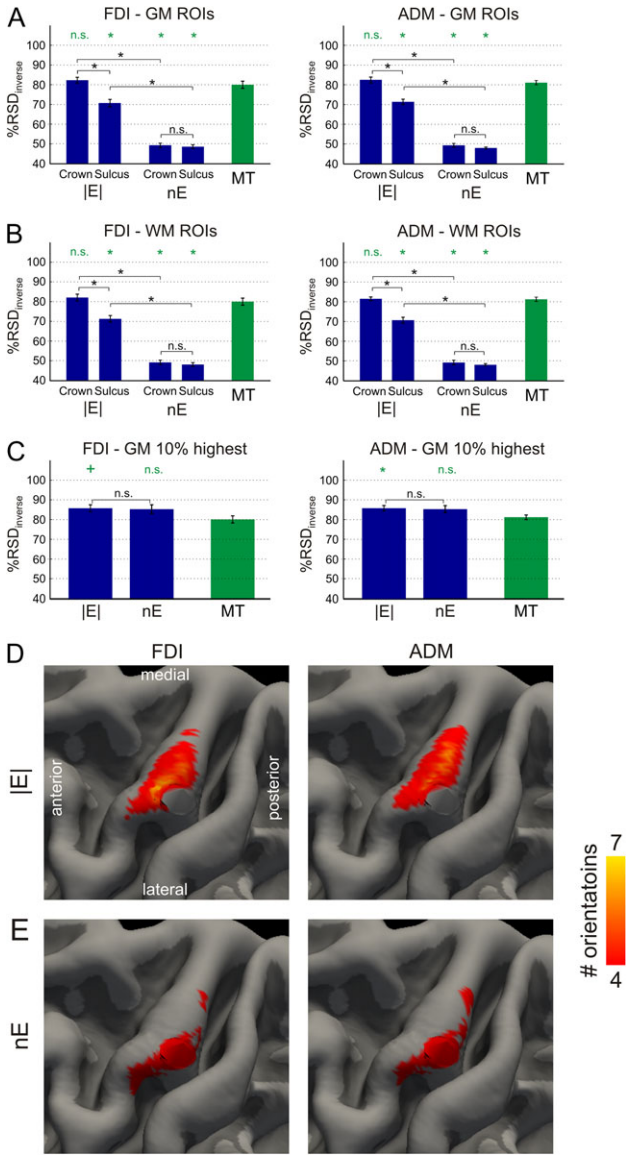

Figure 4. Bar plots of $\%RSD_{inverse}$ (±SE). Left: FDI, right: ADM. The blue bars show $\%RSD_{inverse}$ for the electric field strength **|E|** and the normal component **nE**, respectively. The green bars show $\%RSD_{inverse}$ for the MT alone as reference values. These values correspond to a situation in which the field is independent of the coil orientation. Pair-wise comparisons between conditions of interest were carried out using *t*-tests. The significance level is indicated by * (significant at $P < 0.05$, corrected for multiple comparisons) and + (significant at $P < 0.05$ uncorrected). The pairs are indicated by the brackets. The results of comparisons to the reference $\%RSD_{inverse}$ of the MT are indicated in green. (*A*) Comparison of the mean $\%RSD_{inverse}$ values for **|E|** and **nE** in the GM ROIs as shown in Figure 1B. The values of **nE** are significantly lower than for **|E|**. The values for **|E|** are significantly lower in the sulcal region compared with the gyral crown. All values except for **|E|** at the gyral crown are significantly lower than the reference value for MT. (*B*) Same as A, but using WM ROIs. (*C*) Comparison of the $\%RSD_{inverse}$ values for the highest 10% of **|E|** and **nE**, respectively. In both cases, the values are higher than the reference value for MT. However, only the values for **|E|** reach significance, driven by a more consistent behavior across subjects (i.e., lower SE). (*D*) Topographic distributions of the cortical positions with the highest 10% of the field strength values **|E|**. Shown are average values across subjects on the Freesurfer template. The values indicate how frequently a position experienced the highest field strength (or normal component) when rotating the coil, with 9 being the upper limit for a position that was consistently strongly stimulated for all tested coil orientations (not reached in the group average). Left: FDI, right: ADM. (*E*) Topographic distribution for the peak values of the normal component **nE**.

between field estimates and MEP responses (Thielscher and Kammer 2002; Opitz et al. 2013, 2014).

Third, conclusions on the exact stimulation position (and by that, also on the absolute thresholds in V/m) are hampered by our limited understanding of the TMS effects on the microscopic level, leaving a remaining uncertainty in the range of a few millimeters. In our case, the most consistent correspondence between the biophysical estimates and the physiological thresholds was found when choosing the peak field strength as parameter. This is in line with the observation that the peak values of the normal component (Fig. 4*E*) were consistently found posterior to the CoGs that were situated above the crown of the precentral gyrus (see also, e.g., Herwig et al. 2002; Sparing et al. 2008). That renders stimulation via the normal component less likely, considering that the lowest MTs should then have occurred for coil positions posterior to the CoG (Supplementary Fig. S3 shows an example to illustrate that shifting the coil in posterolateral direction relative to the experimentally determined CoG would increase the strength of the normal component in the sulcal wall). However, testing the assumption that different cortex positions are affected by changing coil orientations resulted in similarly high $\%RSD_{inverse}$ values for the normal component compared with the field strength in superficial parts of the gyrus. That is, while our results help to narrow down the affected area of M1, further progress in the understanding of the TMS effects at the microscopic level is needed to fully leverage the usage of field calculations for planning and dosage control in TMS. Ideally, this will encompass realistic biophysical modeling which combines field calculations with neural models, as started in Salvador et al. (2011), and direct validation measurement in animals (Moliadze et al. 2003; Mueller et al. 2014).

As a critical test of the individual head models, we maximized the impact of the gyral anatomy on the electric field distribution by means of manipulating the coil orientation. Both the electric field in the hand knob region and the physiological response underwent strong variations while keeping the hand knob in the center of stimulation. By demonstrating a reasonable fit between changes in the electric field and changes in MT, our results confirm an acceptable accuracy of the calculated fields. That is in contrast to earlier studies (Opitz et al. 2013; Krieg et al. 2015) which tested the correspondence between MEP responses and field estimates for single coil orientations such that the electric field direction in the hand knob was kept approximately constant. By that, the influence of the anatomy on the field was similar across tested positions and thus less important in modulating the field and the electrophysiological response. Related to this, it was suggested that TMS activates the sulcal wall rather than more superficial parts, and that this is due to an orientation preference of the neural structures with the lowest thresholds when the field direction is normal to the cortical sheet (termed the "cortical column cosine" CCC model; Fox et al. 2004). This was primarily based on the observation of predominantly sulcal activation measured by PET in response to supra-threshold rTMS stimulation. The hypothesis has several weaknesses. First, it was based on PET data obtained for supra-threshold stimulation, in which network effects and afferent sensory feedback caused by the muscle twitches have a strong impact on the activation pattern. In contrast, the strongest activations occurred in superficial parts of the brain underneath the coil center in 2 studies employing subthreshold TMS (Siebner et al. 2001; Takano et al. 2004). Specifically, the average MNI coordinates reported in Fox et al. (2004) for the activations induced by supra-threshold TMS

are x/y/z = −34/−29/50 (using the Talairach-MNI transformation from Lacadie et al. 2008), with a distance of 35 mm to the closest point on the skin (determined using the MNI template and a custom Matlab script). In contrast, Takano et al. (2004) reports the MNI coordinates of the activation peaks due to subthreshold TMS as x/y/z = −24/−20/68 (Takano et al. 2004) and −30/−27/66 (Siebner et al. 2001), which both have distances of 23 mm to their closest skin points. Second, even when applying the CCC model to the calculated electric fields, the most likely activated regions are still not in the sulcus, but—as shown here—at the posterior rim of the gyral crown. This is due to the strong decay of the electric field with depth which outweighs the preference for normal field directions as induced by the cosine weighting function. Third, on a physiological level, we would expect the predominant occurrence of D- rather than I-waves if TMS acted indeed mainly on neural structures in the sulcus. The axons or axon hillocks of the corticospinal pyramidal cells in the sulcal wall likely have low activation thresholds to currents which flow parallel to the brain surface and hit the sulcal wall perpendicularly. These axons are thick and well myelinated, and are starting parallel to the field and then bend away, making the bend a low-threshold point (Amassian et al. 1992). As the axons in the caudal part of M1 directly innervate the spinal motoneurons (Rathelot and Strick 2009), their stimulation would result in D-waves, not I-waves. This is in contrast to the finding that TMS at the optimal coil orientation predominantly evokes I-waves (Di Lazzaro et al. 2008), indicating that the steep decrease in field strength as a function of depth prevents a direct stimulation of those structures. Fourth, in the so far most realistic simulation of TMS-related neural activation by Salvador et al. (2011), both superficial and sulcal neural structures exhibited similar activation thresholds to TMS. That is, given our current knowledge of the activation mechanisms of cortical neural cells, it would be premature to make strong conclusions on putative orientation preferences of cortical structures relative to the currents induced by TMS. Specifically, the prediction of the CCC model that cortical tissue is not at all excitable by tangential currents, as caused by the hypothesized cosine dependence, seems unrealistic from a physiological point of view. In the meantime, the original CCC hypothesis was revised by the proposing group in favor of an alternative that also allows for a strong role of tangential currents in the induction of neural activation (Krieg et al. 2015). It remains to be seen whether a division of the electric field vector into normal and tangential subcomponents relative to the cortical sheet helps to better link the field estimates with physiology compared with simply considering the electric field magnitude. Specifically, it seems unclear whether this can help to explain the differences seen for posterior–anterior (PA) versus anterior–posterior (AP) stimulation.

A consequence of our limited understanding on the activation mechanisms of TMS at the neural level is that we cannot link the results of the field calculations to the observed threshold and latency differences for stimulation with the current flow in the standard PA versus the AP direction (Sakai et al. 1997; Kammer et al. 2001). The induced field distributions are identical for both cases, except for the field vectors being mirrored by 180°. The threshold and latency differences are thus exclusively caused by a different impact of the field on the neural elements, and are not captured when using the electric field strength as parameter for cortical activation. One could assume more complex mathematical dependencies between the electric field and the physiological response in order to also model this effect. However, we opted against their exploration in the current study as their choice is necessarily speculative and potentially misleading as long as better hypotheses on the affected neural structures are missing.

It is worth noting that the different thresholds and latencies for stimulation with PA and AP direction are also not captured by the normal component of the field. For a current flow from anterior to posterior, the normal component of the electric field is negative in large parts of M1. However, the meaning of negative values of the normal component is generally unclear in terms of neural excitation. In principle, they could indicate that the corresponding cortex regions are inhibited rather than excited by TMS. In that case, motor cortex stimulation using currents in AP direction would inhibit most of M1. MEPs would then have to result from the indirect excitation of M1 via the stimulation of premotor areas or the primary sensorimotor cortex, which seems questionable.

To summarize, we are still faced with the challenge to develop a better understanding about the impact of the electric field on the microscopic level that takes the orientation of the neural processes into account. As the stimulation likely occurs close to the gyral crown, the field components tangential to the cortical surface are much stronger than the normal components. This means that cortical orientation alone is unlikely to be a useful macroscopic marker of the orientation of the stimulated neural elements, but that additional factors such as the local connectivity to neighboring areas might have to be taken into account. That is, explaining the MT differences between AP and PA stimulation would require the introduction of additional, rather speculative assumptions on the type and orientation of neural elements which are predominantly affected. Further insight might come from studies using invasive recording to decipher the TMS effects on the neural level (Mueller et al. 2014) which in turn might allow us to introduce stronger hypotheses on the link between the induced electric field and neural excitation.

While we could explain a significant amount of the MT changes by means of electric field changes, the observed fit might have been limited due to several factors. First, the incomplete understanding of the TMS effects on the microscopic level together with the number of data points in each subject (9 coil orientations) forced us to test rather basic mathematical dependencies between the field and the physiological response in order to avoid overfitting. We therefore opted to keep the tested dependencies as simple as possible and carefully motivated by prior findings and existing hypotheses. For example, even when stimulating at MT, we cannot rule out that the physiological response at least in some cases stemmed from the simultaneous excitation of several subareas of M1. In that sense, it might well be that we missed some “auxiliary” subareas which might have contributed to the observed MT profile to some extent. Thus, while restricting this study to the test of simple mathematical dependencies, it might be interesting to reassess the data once better hypotheses on the affected neural structures are available. Other factors that might have limited the fit between field and MT changes are noise in the MT measurements (caused, e.g., by slight variations in the pre-contraction level) and uncertainties on the tissue conductivities that have been assumed in the FEM calculations. Uncertainties in the conductivities of the skin and skull are of less importance for TMS field calculations as the induced fields are in general oriented parallel to the inner skull boundary. The variability of the conductivity of CSF is probably low (Baumann et al. 1997; Vorwerk et al. 2014), while there is some uncertainty on the values for GM and WM (Thielscher et al. 2011). However,

the general impact of the gyrification on the electric field distribution has been shown to be robust to this uncertainty (Thielscher et al. 2011) so that we can expect that the results presented here are stable.

In conclusion, we demonstrated a significant correspondence between electric field calculations based on realistic head models and MT changes. The best correspondence was consistently seen in the crown region of the precentral gyrus and was robust to the assumptions made for the neural activation model. Using simplified head models similar to spherical head models resulted in spatially unspecific findings. Our results suggest that the maximum electric field strength is currently the best parameter to use when further exploring the usability of field calculations for quantitative dosing. They also show that a clearer understanding of the TMS effects on the neural elements is required to allow for a better interpretation of the calculated fields.

Supplementary Material

Supplementary material can be found at: http://www.cercor.oxfordjournals.org/

Funding

Lundbeckfonden (PI: Axel Thielscher; Grant No. R118-A11308), a "Grant of Excellence" sponsored by Lundbeckfonden (PI: Hartwig Siebner; Grant No. R59 A5399), an Interdisciplinary Synergy Grant "Basics" sponsored by NovoNordisk fonden (recipients: Hartwig Siebner, Axel Thielscher & Lars K Hansen, Grant No. 11413), a project grant sponsored by the German Federal Ministry for Economic Affairs and Energy (PI: Axel Thielscher; Grant No. KF2881001KJ1) and a project grant sponsored by the German Research Foundation (DFG; PI: Axel Thielscher, Grant No. TH1330/4-1).

Notes

We would like to thank the anonymous reviewers for their constructive feedback which helped to improve the paper.

References

Amassian VE, Eberle L, Maccabee PJ, Cracco RQ. 1992. Modelling magnetic coil excitation of human cerebral cortex with a peripheral nerve immersed in a brain-shaped volume conductor: the significance of fiber bending in excitation. Electroencephalogr Clin Neurophysiol. 85:291–301.

Barker AT, Jalinous R. 1985. Non-invasive magnetic stimulation of human motor cortex. Lancet. 1:1106–1107.

Baumann SB, Wozny DR, Kelly SK, Meno FM. 1997. The electrical conductivity of human cerebrospinal fluid at body temperature. IEEE Trans Biomed Eng. 44:220–223.

Classen J, Benecke R. 1995. Inhibitory phenomena in individual motor units induced by transcranial magnetic stimulation. Electroencephalogr Clin Neurophysiol. 97:264–274.

Dannhauer M, Lanfer B, Wolters CH, Knösche TR. 2011. Modeling of the human skull in EEG source analysis. Hum Brain Mapp. 32:1383–1399.

Di Lazzaro V, Ziemann U, Lemon RN. 2008. State of the art: physiology of transcranial motor cortex stimulation. Brain Stimul. 1:345–362.

Dular P, Geuzaine C, Henrotte F, Legros W. 1998. A general environment for the treatment of discrete problems and its application to the finite element method. IEEE Trans Magn. 34:3395–3398.

Fischl B, Sereno MI, Tootell RBH, Dale AM. 1999. High-resolution intersubject averaging and a coordinate system for the cortical surface. Hum Brain Mapp. 8:272–284.

Fox PT, Narayana S, Tandon N, Sandoval H, Fox SP, Kochunov P, Lancaster JL. 2004. Column-based model of electric field excitation of cerebral cortex. Hum Brain Mapp. 22:1–14.

Friston KJ, Buechel C, Fink GR, Morris J, Rolls E, Dolan RJ. 1997. Psychophysiological and modulatory interactions in neuroimaging. NeuroImage. 6:218–229.

Geyer S, Ledberg A, Schleicher A, Kinomura S, Schormann T, Burgel U, Klingberg T, Larsson J, Zilles K, Roland PE. 1996. Two different areas within the primary motor cortex of man. Nature. 382:805–807.

Geyer S, Matelli M, Luppino G, Zilles K. 2000. Functional neuroanatomy of the primate isocortical motor system. Anat Embryol. 202:443–474.

Greve DN, Fischl B. 2009. Accurate and robust brain image alignment using boundary-based registration. Neuroimage. 48:63–72.

Güllmar D, Haueisen J, Reichenbach JR. 2010. Influence of anisotropic electrical conductivity in white matter tissue on the EEG/MEG forward and inverse solution. A high-resolution whole head simulation study. Neuroimage. 51:145–163.

Herwig U, Kölbel K, Wunderlich AP, Thielscher A, von Tiesenhausen C, Spitzer M, Schönfeldt-Lecuona C. 2002. Spatial congruence of neuronavigated transcranial magnetic stimulation and functional neuroimaging. Clin Neurophysiol. 113:462–468.

Huang Y-Z, Edwards MJ, Rounis E, Bhatia KP, Rothwell JC. 2005. Theta burst stimulation of the human motor cortex. Neuron. 45:201–206.

Ilmoniemi RJ, Ruohonen J, Karhu J. 1999. Transcranial magnetic stimulation—a new tool for functional imaging of the brain. Crit Rev Biomed Eng. 27:241–284.

Kammer T, Beck S, Thielscher A, Laubis-Herrmann U, Topka H. 2001. Motor thresholds in humans. A transcranial magnetic stimulation study comparing different pulseforms, current directions and stimulator types. Clin Neurophysiol. 112:250–258.

Krieg TD, Salinas FS, Narayana S, Fox PT, Mogul DJ. 2015. Computational and experimental analysis of TMS-induced electric field vectors critical to neuronal activation. J Neural Eng. 12:046014.

Kujirai T, Caramia M, Rothwell J, Day B, Thompson P, Ferbert A, Wroe S, Asselman P, Marsden CD. 1993. Corticocortical inhibition in human motor cortex. J Physiol. 471:501–519.

Lacadie CM, Fulbright RK, Rajeevan N, Constable RT, Papademetris X. 2008. More accurate Talairach coordinates for neuroimaging using non-linear registration. Neuroimage. 42:717–725.

Maccabee PJ, Amassian VE, Eberle LP, Cracco RQ. 1993. Magnetic coil stimulation of straight and bent amphibian and mammalian peripheral nerve in vitro: locus of excitation. J Physiol. 460:201–219.

Maccabee PJ, Nagarajan SS, Amassian VE, Durand DM, Szabo AZ, Ahad AB, Cracco RQ, Lai KS, Eberle LP. 1998. Influence of pulse sequence, polarity and amplitude on magnetic stimulation of human and porcine peripheral nerve. J Physiol. 513:571–585.

Moliadze V, Zhao YQ, Eysel U, Funke K. 2003. Effect of transcranial magnetic stimulation on single-unit activity in

the cat primary visual cortex. J Physiol (London). 553: 665–679.

Mueller JK, Grigsby EM, Prevosto V, Petraglia FW, Rao H, Deng ZD, Peterchev AV, Sommer MA, Egner T, Platt ML, et al. 2014. Simultaneous transcranial magnetic stimulation and single-neuron recording in alert non-human primates. Nat Neurosci. 17:1130–1136.

Opitz A, Legon W, Rowlands A, Bickel WK, Paulus W, Tyler WJ. 2013. Physiological observations validate finite element models for estimating subject-specific electric field distributions induced by transcranial magnetic stimulation of the human motor cortex. Neuroimage. 81:253–264.

Opitz A, Windhoff M, Heidemann RM, Turner R, Thielscher A. 2011. How the brain tissue shapes the electric field induced by transcranial magnetic stimulation. Neuroimage. 58: 849–859.

Opitz A, Zafar N, Bockermann V, Rohde V, Paulus W. 2014. Validating computationally predicted TMS stimulation areas using direct electrical stimulation in patients with brain tumors near precentral regions. Neuroimage Clin. 4:500–507.

Pascual-Leone A, Vallssole J, Wassermann EM, Hallett M. 1994. Responses to rapid-rate transcranial magnetic stimulation of the human motor cortex. Brain. 117:847–858.

Raffin E, Pellegrino G, Di Lazzaro V, Thielscher A, Siebner HR. 2015. Bringing transcranial mapping into shape: Sulcus-aligned mapping captures motor somatotopy in human primary motor hand area. Neuroimage. doi:10.1016/j.neuroimage.2015.07.024.

Rathelot JA, Strick PL. 2009. Subdivisions of primary motor cortex based on cortico-motoneuronal cells. Proc Natl Acad Sci U S A. 106:918–923.

Rattay F. 1998. Analysis of the electrical excitation of CNS neurons. IEEE Trans Biomed Eng. 45:766–772.

Rossini PM, Burke D, Chen R, Cohen LG, Daskalakis Z, Di Iorio R, Di Lazzaro V, Ferreri F, Fitzgerald PB, George MS, et al. 2015. Non-invasive electrical and magnetic stimulation of the brain, spinal cord, roots and peripheral nerves: basic principles and procedures for routine clinical and research application. An updated report from an IFCN Committee. Clin Neurophysiol. 126:1071–1107.

Sakai K, Ugawa Y, Terao Y, Hanajima R, Furubayashi T, Kanazawa I. 1997. Preferential activation of different I waves by transcranial magnetic stimulation with a figure-of-eight-shaped coil. Exp Brain Res. 113:24–32.

Salvador R, Silva S, Basser PJ, Miranda PC. 2011. Determining which mechanisms lead to activation in the motor cortex: a modeling study of transcranial magnetic stimulation using realistic stimulus waveforms and sulcal geometry. Clin Neurophysiol. 122:748–758.

Siebner HR, Takano B, Peinemann A, Schwaiger M, Conrad B, Drzezga A. 2001. Continuous transcranial magnetic stimulation during positron emission tomography: a suitable tool for imaging regional excitability of the human cortex. Neuroimage. 14:883–890.

Smith SM, Jenkinson M, Woolrich MW, Beckmann CF, Behrens TEJ, Johansen-Berg H, Bannister PR, Luca MD, Drobnjak I, Flitney DE, et al. 2004. Advances in functional and structural MR image analysis and implementation as FSL. NeuroImage. 23:S208–S219.

Sparing R, Buelte D, Meister IG, Paus T, Fink GR. 2008. Transcranial magnetic stimulation and the challenge of coil placement: a comparison of conventional and stereotaxic neuronavigational strategies. Hum Brain Mapp. 29:82–96.

Stefan K, Kunesch E, Cohen LG, Benecke R, Classen J. 2000. Induction of plasticity in the human motor cortex by paired associative stimulation. Brain. 123:572–584.

Stepniewska I, Preuss TM, Kaas JH. 1993. Architectonics, somatotopic organization, and ipsilateral cortical connections of the primary motor area (M1) of owl monkeys. J Comp Neurol. 330:238–271.

Takano B, Drzezga A, Peller M, Sax I, Schwaiger M, Lee L, Siebner HR. 2004. Short-term modulation of regional excitability and blood flow in human motor cortex following rapid-rate transcranial magnetic stimulation. Neuroimage. 23:849–859.

Thielscher A, Antunes A, Saturnino GB. 2015. Field modeling for transcranial magnetic stimulation: a useful tool to understand the physiological effects of TMS? Annual International Conference of the IEEE Engineering in Medicine and Biology Society 2015. Milan, Italy.

Thielscher A, Kammer T. 2002. Linking physics with physiology in TMS: a sphere field model to determine the cortical stimulation site in TMS. NeuroImage. 17:1117–1130.

Thielscher A, Kammer T. 2004. Electric field properties of two commercial figure-8 coils in TMS: calculation of focality and efficiency. Clin Neurophysiol. 115:1697–1708.

Thielscher A, Opitz A, Windhoff M. 2011. Impact of the gyral geometry on the electric field induced by transcranial magnetic stimulation. Neuroimage. 54:234–243.

Truong DQ, Magerowski G, Blackburn GL, Bikson M, Alonso-Alonso M. 2013. Computational modeling of transcranial direct current stimulation (tDCS) in obesity: impact of head fat and dose guidelines. Neuroimage Clin. 2:759–766.

Tuch DS, Wedeen VJ, Dale AM, George JS, Belliveau JW. 2001. Conductivity tensor mapping of the human brain using diffusion tensor MRI. Proc Natl Acad Sci U S A. 98:11697–11701.

Vorwerk J, Cho JH, Rampp S, Hamer H, Knosche TR, Wolters CH. 2014. A guideline for head volume conductor modeling in EEG and MEG. Neuroimage. 100:590–607.

Windhoff M, Opitz A, Thielscher A. 2013. Field calculations in brain stimulation based on finite elements: an optimized processing pipeline for the generation and usage of accurate individual head models. Hum Brain Mapp. 34:923–935.

Worsley K, Marrett S, Neelin P, Vandal A, Friston K, Evans A. 1996. A unified statistical approach for determining significant voxels in images of cerebral activation. Hum Brain Mapp. 4:58–73.

Yamashita A, Arikuni T. 2001. Axon trajectories in local circuits of the primary motor cortex in the macaque monkey (Macaca fuscata). Neurosci Res. 39:233–245.

Yousry TA, Schmid UD, Alkadhi H, Schmidt D, Peraud A, Buettner A, Winkler P. 1997. Localization of the motor hand area to a knob on the precentral gyrus—a new landmark. Brain. 120:141–157.